Journal of Materials Chemistry A

Accepted Manuscript

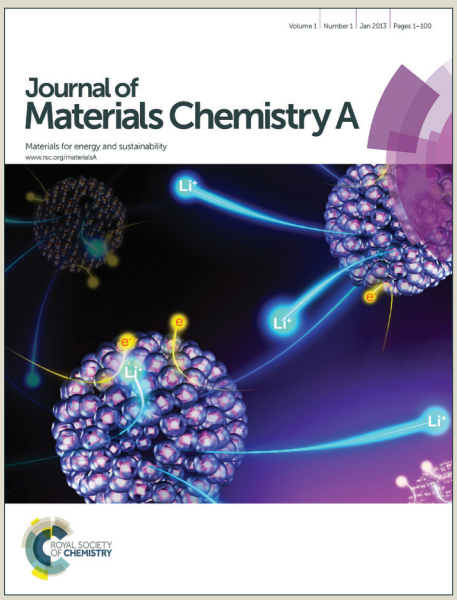

ROYAL SOCIETY OF CHEMISTRY

www.rsc.org/materialsA

Graphical Abstract

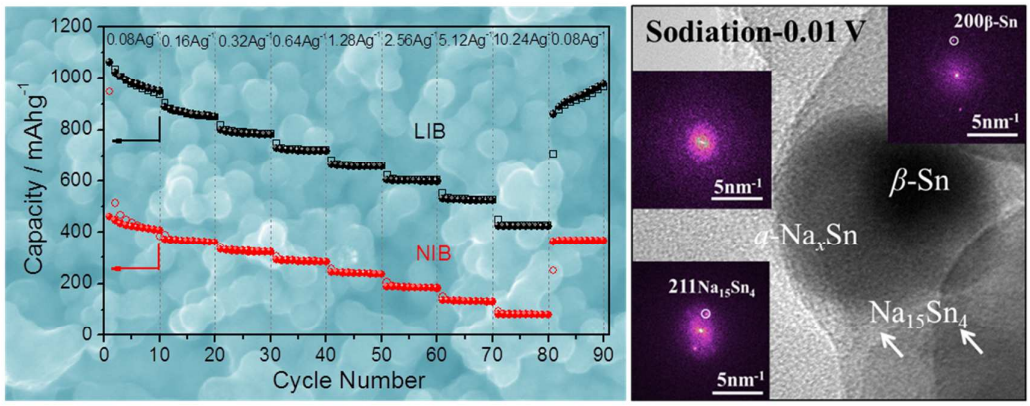

Sodiation vs. Lithiation Phase Transformations in a High Rate - High Stability SnO_2 in Carbon Nanocomposite

Jia Ding[a*], *Zhi Li*[a], *Huanlei Wang*[a], *Kai Cui*[b], *Alireza Kohandehghan*[a], *Xuehai Tan*[a], *Dimitre Karpuzov*[c], *David Mitlin*[d,a*]

[a]Chemical and Materials Engineering, University of Alberta, Edmonton, Alberta T6G 2V4, Canada
[b]National Institute for Nanotechnology (NINT), National Research Council of Canada, Edmonton, Alberta T6G 2M9, Canada
[c] Alberta Center for Surface Engineering and Science (ACSES), University of Alberta, Edmonton, AB, Canada T6G 2G6
[d] Chemical & Biomolecular Engineering and Mechanical Engineering, Clarkson University, Potsdam, NY, USA 13699

*Address correspondence to dingjiasiom@gmail.com (J. Ding); dmitlin@clarkson.edu (D. Mitlin).

Abstract

We employed a glucose mediated hydrothermal self-assembly method to create a SnO_2 - carbon nanocomposite with promising electrochemical performance as both a sodium and a lithium ion battery anode (NIBs NABs SIBs, LIBs), being among the best in terms of cyclability and rate capability when tested against Na. In parallel we provide a systematic side-by-side comparison of the sodiation *vs*. lithiation phase transformations in nano SnO_2. The high surface area (338 m^2g^{-1}) electrode is named C-SnO_2, and consists of a continuous Li and Na active carbon frame with internally imbedded sub-5nm SnO_2 crystallites of high mass loading (60 wt.%). The frame imparts excellent electrical conductivity to the electrode, allows for rapid diffusion of Na and Li ions, and carries the sodiation/lithiation stresses while preventing

cycling-induced agglomeration of the individual crystals. C-SnO_2 employed as a NIB anode displays a reversible capacity of 531 $mAhg^{-1}$ (at 0.08 Ag^{-1}) with 81% capacity retention after 200 cycles, while capacities of 240, 188 and 133 $mAhg^{-1}$ are achieved at the much higher rates of 1.3, 2.6 and 5 Ag^{-1}. As a LIB anode C-SnO_2 maintains a capacity of 1367 $mAhg^{-1}$ (at 0.5 Ag^{-1}) after 400 cycles, and 420 $mAhg^{-1}$ at 10 Ag^{-1}. Combined TEM, XRD and XPS prove that the much lower capacity of SnO_2 as a NIB anode is due to the kinetic difficulty of the Na - Sn alloying reaction to reach the terminal $Na_{15}Sn_4$ intermetallic, whereas for Li - Sn the $Li_{22}Sn_5$ intermetallic is readily formed at 0.01V. Rather, with applied voltage a significant portion of the material effectively shuffles between SnO_2 and β-Sn + NaO_2. The conversion reaction proceeds differently in the two systems: LiO_2 is reduced directly to SnO_2 and Li, whereas the NaO_2 to SnO_2 reaction proceeds through an intermediate SnO phase.

Key words: SnO_2, Sn, conversion, SIB, NIB, NAB, LIB, battery, capacitor

Introduction

Electrical energy storage systems are critical technologies to address the global energy shortage and emerging environmental issues. As one of the most important EES systems, lithium ion batteries (LIBs), have been widely applied in electric vehicles, portable devices and grid storages.[1,2,3] Due to the increasing concern about lithium's cost and continued availability, sodium ion batteries (NIBs) are currently

under extensive investigation as an alternative to LIBs.[4,5,6,7,8,9,10,11] There have been good recent successes in developing NIB cathodes[12,13,14,15]. Moreover, highly ordered but non-graphitic carbons,[16,17,18,19] titanium oxides/compounds[20,21,22,23] and alloys[24,25,26,27,28,29] are emerging promising NIB anode materials. Candidates for alloy - dealloying anodes include Sn,[30,31,32] Si,[33,34,35] Ge,[36] Sb,[37,38] SnO_x,[39,40,41,42,43,44,45,46] Sb_2O_3[47,48] etc.

Tin dioxide (SnO_2) is a promising LIB anode material, which has recently been applied to the Na system.[41,49,50,51,52,53,54,55,56] In a LIB application, based on systematic *in-situ* TEM,[57] atomic scale HRTEM characterization[58] and *ex-situ* XPS, TEM analysis[52], it is commonly proposed that the charge storage mechanism of SnO_2 is based on a reversible conversion reaction ($SnO_2 + 4Li + 4e^- \leftrightarrow Sn + Li_2O$) combined with an alloying reaction ($Sn + 4.4Li^+ + 4.4e^- \leftrightarrow Li_{22}Sn_5$),[58] resulting to a theoretical capacity of 1494 $mAhg^{-1}$ for the combined reactions. In the recent studies applying SnO_2 as LIBs anode, the practical capacities obtained have generally been in that range.[51,52,59] With Na the capacity should be only somewhat lower (1378 $mAhg^{-1}$, assuming that SnO_2 follows a parallel conversion ($SnO_2 + 4Na^+ + 4e^- \leftrightarrow Sn + Na_2O$, 711 $mAhg^{-1}$), and then an alloying reaction ($Sn + 3.75Na^+ + 3.75e^- \leftrightarrow Na_{15}Sn_4$, 667 $mAhg^{-1}$ normalized to the mass of SnO_2).[60] By contrast for the case of Na, the experimentally measured capacity of SnO_2 based materials are generally much lower than the theoretical value.[54,55,61,62,63,64] To date this discrepancy remains unresolved, and it would be desirable to test and analyze the same material against Na and against

Li to ascertain the key mechanistic differences in the charging - discharging behavior.

A key issue for broad range of NIB anode materials is that they appear to undergo significant capacity fading during cycling, on a scale that is substantially worse than for comparable LIB anodes. While there may be numerous reasons for this degradation, the commonly observed factors in both LIBs and NIBs are material pulverization (loss of electrical contact) and/or agglomeration of nanoparticulates (worsening of kinetics due to loss of nano-scale diffusion distances).[65] For the oxides (*e.g.* SnO_2) especially, material agglomeration will also impede the reversibility of the conversion reaction.[51,52] In order to minimize this problem, researchers introduce secondary carbon phases (*e.g.* CNT,[66,67] graphene,[40,51,68,69] carbon fibers,[70,71] disordered carbon,[72,73] *etc.*) that both accommodate the volume expansion and prevent the aggregation of the active materials. Substantial success has been achieved applying this strategy for LIBs, with this approach becoming applied for NIBs as well.[27,61,74] However NIB anodes undergo a larger volumetric expansion than their LIB counterparts (due to the larger diameter of the former ion: 1.06 Å Na *vs*. 0.76 Å).[75] This raises a bigger challenge in buffering the stress during sodiation and in preventing the capacity decay due to the materials pulverization/agglomeration issues.

In this work, we prepared a unique nanostructured SnO_2 - carbon composite through a self-assembly process under hydrothermal conditions. The C-SnO_2 electrode exhibited quite promising electrochemical performance as anodes for both

NIBs and LIBs. We systemically investigated the phase transformations associated with SnO_2 reacting with Na, providing a systematic and broadly applicable picture of the origin of the capacity difference of this material for NIB *vs*. for LIB applications.

Experimental Procedure

Materials Preparation

C-SnO_2 materials were prepared by a modified hydrothermal synthesis method followed by a carbonization process. In a typical synthesis, hexadecyltrimethylammonium bromide (CTAB, $(C_{16}H_{33})N(CH_3)_3Br$, 0.5g) was firstly dispersed in 15mL MQ-water. After stirring for 2h, 1.2g glucose was dissolved afterwards. Finally, 0.35g sodium stannate (Na_2SnO_3) trihydrate was dissolved in the former solution under vigorously stirring for 0.5h. Then the final aqueous solution was placed in a 50 mL stainless steel autoclave. The autoclave was sealed, soaked at 160°C for 1h and at 180°C for another 1.5h before it was allowed to cool to room temperature. The reaction mechanism of stannate hydrolysis under the modified hydrothermal condition will be further discussed in the Results and Discussion section. The resulting brown product was thoroughly washed by both ethanol and MQ-water, then collected by filtration and dried at 80°C overnight. The further carbonization is carried out in a horizontal tube furnace at 510°C for 3h under argon flow. SnO_2 nanoparticle baseline was prepared by the same procedure but without glucose and CTAB. The pure carbon reference was prepared without CTAB and stannate salt.

Material Characterization

For the morphologies of the material, a Hitachi S-4800 SEM equipped with field emission gun is used. TEM analysis is performed using a JEOL JEM-2010 TEM, with an accelerating voltage of 200 kV. XRD analysis was performed using a Bruker AXS D8 Discover diffractometer with the Cu K_{α} radiation. XPS spectra were obtained on an Axis Ultra spectrometer. Nitrogen adsorption-desorption analysis was performed using Quantachrome Instruments (U.S.A) Autosorb-1 at 77 K. Thermogravimetric analysis (TGA, Perkin-Elmer TGA 4000) was measured with a heating rate of 5°C min^{-1} under 200 mL min^{-1} of flowing air.

Electrochemical Measurements

Electrochemical tests were carried out using coin cell CR2032. Typically, a slurry of 80% active materials, 10% carbon black (Super-P), and 10% poly(vinlylidenedifluoride) in N-methylpyrrolidone was coated onto a stainless steel disk and then dried at 110°C overnight in a vacuum oven. The mass loading of the electrodes was 1.5 mg cm^{-2}. For Na half cells, Na metal was used as counter electrode and separated from the working electrode with polyethene separator. 1 M $NaClO_4$ dissolved in a mixture of ethylene carbonate (EC) and diethyl carbonate (DEC) with a volume ratio of 1:1 was utilized as the electrolyte. For Li half cells, Li metal as used as counter electrode, 1M $LiPF_6$ solvated in EC-DEC-DMC (dimethyl carbonate), 1:1:1 volumetric ratio was used as electrolyte. All the cyclic voltammetry measurements were conducted on a Solartron 1470 Multistat system. The

galvanostatic charge-discharge tests were performed using an Arbin BT2000 Potentiostat. Before the CV, galvanostatic cycling and rate performance tests, the assembled batteries were first stored at ambient for 8 hours. All electrochemical tests were conducted at room temperature.

Results and Discussion

As-synthesized microstructure

The nanocomposite was prepared through one-pot hydrothermal synthesis, followed by annealing in Ar. Sodium stannate is a commonly employed precursor for SnO_2 materials synthesis.[76,77,78,79] Firstly, after being dissolved in aqueous solution the Na_2SnO_3 is dissociated into ions of Na^+ and SnO_3^{2-}. The hydrothermal treatment of glucose would create a mild acidic condition in the reaction system.[80] In this environment, SnO_3^{2-} would react with H_2O (*i.e.* hydrolysis) forming precipitate particles[81], which would be amorphous tin oxides or tin hydrates. The reaction routes have been described as $SnO_3^{2-} + 3H_2O \rightarrow Sn(OH)_4 + 2OH^-$, or $SnO_3^{2-} + H_2O \rightarrow SnO_2 + 2OH^-$[76,81], with the hydrates transforming into oxides during the subsequent annealing process.[81] Based on the ultimate morphology of the resultant SnO_2 crystals, the pristine hydrolysis products should be sub-5nm in size. Precipitation of carbon-rich polysaccharide took place following stannate hydrolysis, resulting in a self-assembled hierarchical nanostructure of the two phases. The Ar annealing at the relatively low temperature (510°C) further carbonized the polysaccharide but without reducing the oxide. The obtained material consisted of SnO_2 nanoparticle assemblies

embedded in a continuous matrix of amorphous carbon and is termed "C-SnO_2". For a baseline we synthesized carbon-free SnO_2 nanoparticle specimens, naming them "SnO_2".

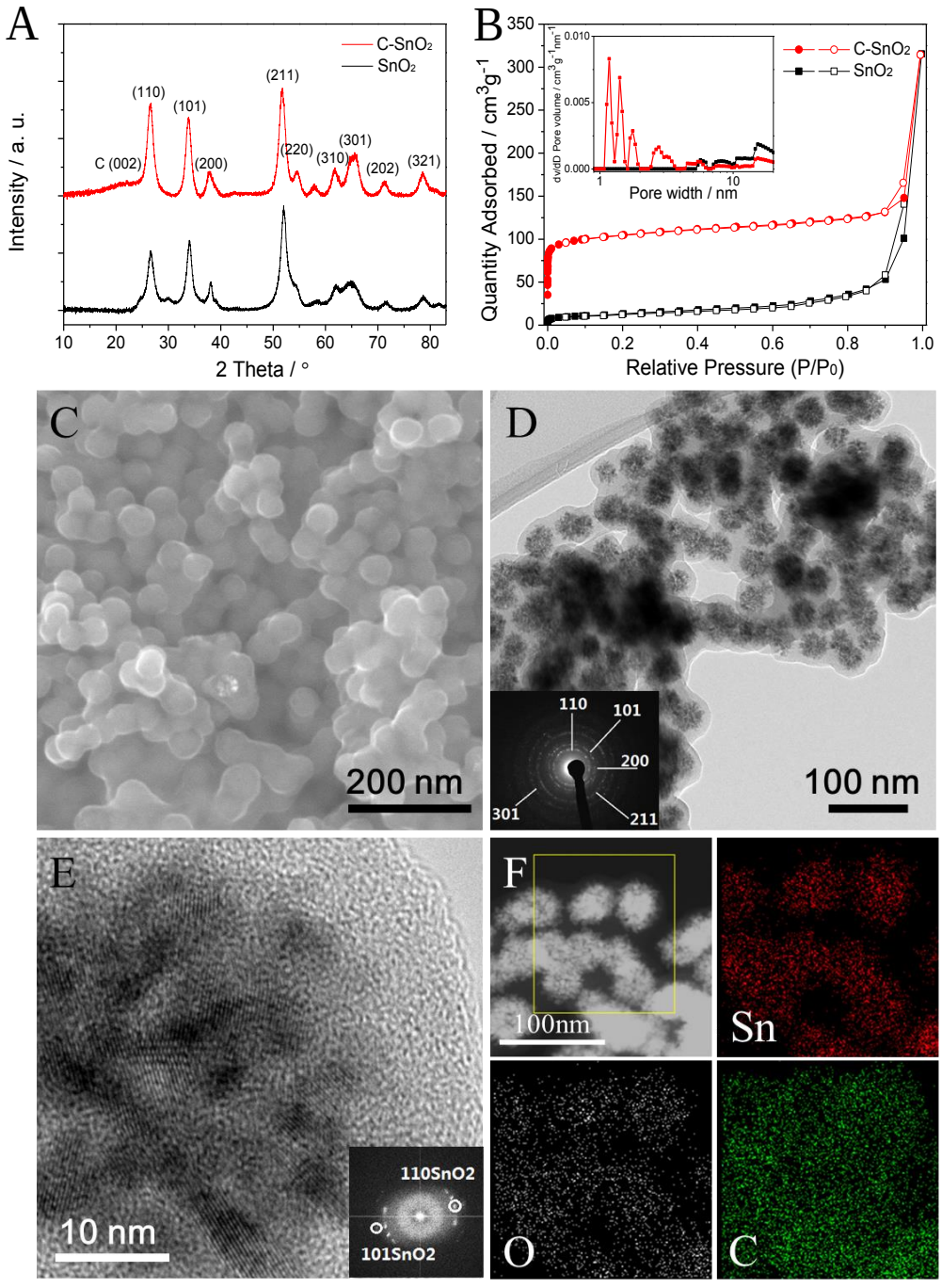

Figure 1: As-synthesized microstructures. (A) Indexed XRD pattern of C-SnO_2 and SnO_2 specimens, showing SnO_2 being present as the rutile phase. (B) Nitrogen adsorption-desorption isotherms of C-SnO_2 and SnO_2, and pore size distribution of both specimens (insert). (C) SEM micrograph revealing the continuous macroscopic

morphology of the nanocomposite. (D) Conventional bright field TEM micrograph and indexed SAD further highlighting the highly interconnected architecture with rutile SnO_2 phase embedded in the carbon. (E) HRTEM micrograph of one such cluster of SnO_2 nanocrystallites within the carbon. (F) HAADF TEM micrograph and EELS elemental maps of Sn, O and C.

The crystalline structure of both C-SnO_2 and SnO_2 was characterized by X-ray diffraction (XRD). As shown in Figure 1A, the patterns of both specimens are indexed as rutile SnO_2,[82] with no other Sn oxide phases being detected (*e.g.* SnO, orthorhombic SnO_2). The broad hump centered at ~22° for C-SnO_2 is due to the carbon. As the carbon phase in C-SnO_2 is highly structurally disordered, it does not possess a graphitic structure and has few intact graphene planes. However, there is short-range order between nearest – neighbor C atoms, with their relative positions being described by a radial distribution of distances. Because there is a frequency maximum in the radial distribution of first and second nearest neighbors, the XRD pattern contains two broad humps (rather than sharp Bragg peaks), with first one being much more intense.[83] In amorphous carbons the first hump occurs at roughly 22°, and may be extrapolated to yield the mean C nearest neighbor position in the disordered array similarly to the way Bragg's law may be employed for long-range ordered phases.

The weight percent of SnO_2 in C-SnO_2 is 60wt%, as evaluated by thermogravimetric analysis (TGA) performed in air and shown in Figure S1A (Supplemental). Combustion of the carbon occurs in the range of 310 - 500°C, with no additional changes in weight at higher temperatures. Figure 1B shows the nitrogen

adsorption-desorption isotherms of C-SnO_2 and SnO_2 specimens. The corresponding pore size distribution results (obtained by density functional theory (DFT)) are shown in the figure insert. C-SnO_2 displays type I isotherm, with a high specific BET surface area of 338 m^2g^{-1} and total pore volume of 0.48 cm^3g^{-1}. Most of the porosity is located in the micro and sub-3nm mesopore regime. Conversely, the SnO_2 specimen possesses a surface area of 48 m^2g^{-1} and inter-particle voids larger than 10 nm. The near-surface structure of C-SnO_2 was characterized by X-ray photoelectron spectroscopy (XPS). Figure S1B displays its survey spectrum, while the insert shows the high resolution spectrum of the Sn 3d double peaks. The peaks at 487 eV and 495.5 eV are ascribed to Sn $3d_{5/2}$ and Sn $3d_{3/2}$ respectively. These peak positions are characteristic of the Sn^{4+} chemical state, further confirming the oxidation state of Sn as SnO_2.

Figure 1C is a SEM micrograph showing a low magnification image of C-SnO_2. On a macroscopic scale the material displays a highly interconnected morphology, reminiscent of a dense coral reef. Figure 1D shows a conventional bright field TEM micrograph and the corresponding indexed selected area diffraction pattern (SAD). The image further highlights the highly interconnected architecture of C-SnO_2, which contains dense assemblies sub-5 nm rutile SnO_2 nanocrystals encapsulated by carbon. Figure 1E shows a HRTEM micrograph of one such assembly containing numerous nanocrystallites. As illustrated by the HAADF TEM micrographs and EELS elemental maps shown in Figure 1F, the assemblies are 50 – 70 nm in scale, with more carbon

between them. As shown in Figure S2, baseline SnO_2 consists of nearly spherical particles in the size range of around 25 nm, without any additional features.

Electrochemical Performance and Phase Transformations *vs*. Li

C-SnO_2 and SnO_2 were tested as half-cells against Li and Na in the range of 0.01 to 3 V and at 0.01 to 1.5 V *vs*. Li/Li^+ or *vs*. Na/Na^+. The mass loading of the electrodes was 1.5 mg cm^{-2}. As most published literature data on SnO_2 is based on approximately the 0.01 to 3 V range, those results are used for the performance comparisons. For each literature comparison we will list the actual voltage window employed in that study. Since testing is being done of half-cells rather than of full batteries, lithiation (sodiation) is defined as "discharge", while delithiation (desodiation) is defined as "charge". For C-SnO_2 the specific capacity is always calculated based on the weight of both the SnO_2 and the carbon. A reversible capacity is defined as the capacity at delithiation/desodiation.

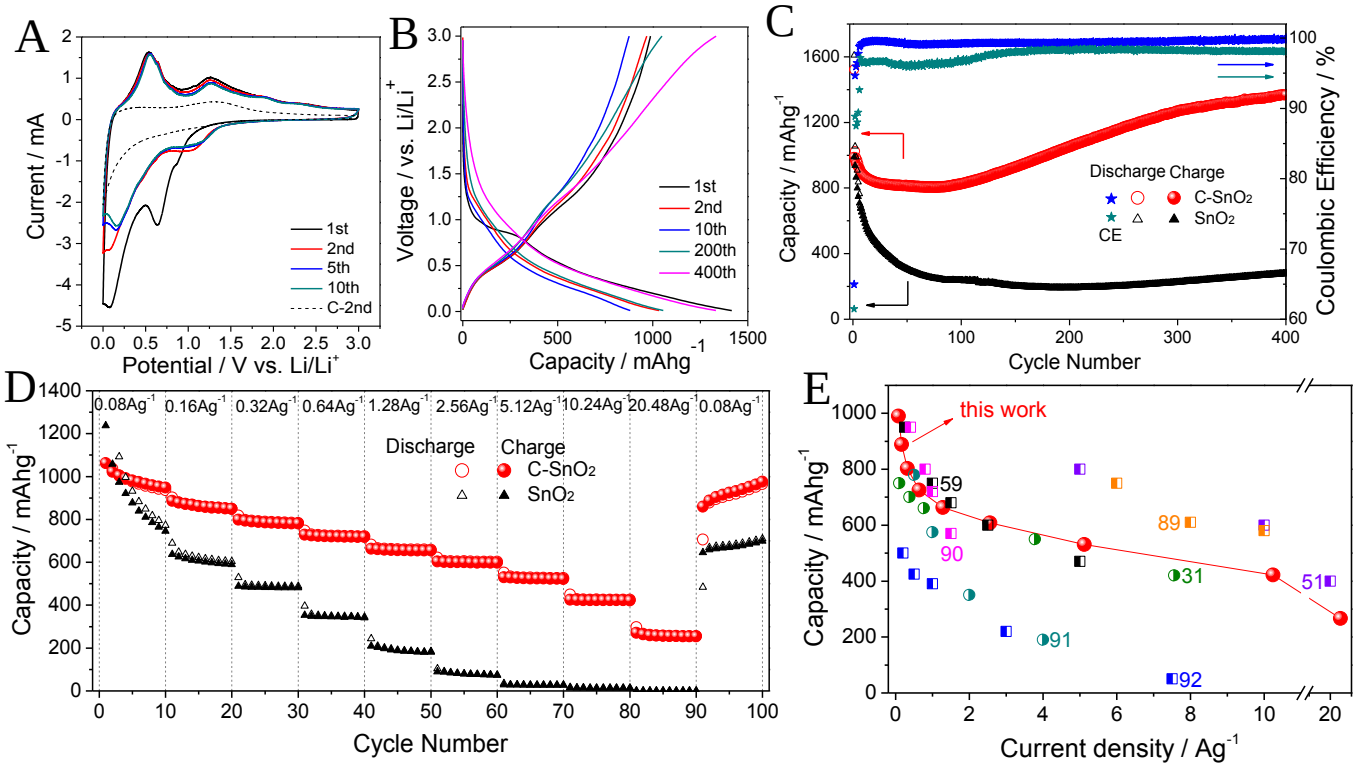

Figure 2: Electrochemical performance of C-SnO_2 versus Li, tested between 0.01 and 3V. (A) Cyclic voltammograms (CVs) at 0.1 mVs^{-1} for the first 10 cycles, also showing the 2nd CV of the baseline pure carbon. (B) Galvanostatic discharge/charge profiles at 0.5 Ag^{-1} for cycles 1 – 400. (C) Cycling performance of C-SnO_2 and SnO_2 (0.5 Ag^{-1}), with corresponding coulombic efficiency (CE) displayed on the right axis. (D) Rate performance of C-SnO_2 and SnO_2. Other electrochemical results for baseline SnO_2 are presented in Figures S3. (E). Rate capability comparison of C-SnO_2 with state-of-the-art SnO_2(◧), Sn (◑) based LIBs anodes from literature. All plotted literature capacities were obtained from tests also performed with a 0.01-3V voltage window.

The lithiation results are presented first. Figure 2A shows the cyclic voltammograms (CVs) of C-SnO_2 electrode for the initial 10 cycles, at a scan rate of 0.1 mVs^{-1}. Also shown is the 2nd CV of the pure carbon phase, employed as a baseline to help identify the Sn and SnO_2 - specific redox peaks. As supported by XRD analysis shown later, the lithiation peak at 1.1V and the delithiation peak at 1.25V correspond to the reversible conversation reaction of tin oxide when it is truly

nanostructured: $SnO_2 + 4Li^+ + 4e^- \leftrightarrow Sn + 2Li_2O$. The position and the relative intensity of the conversion reaction peaks is almost constant between cycle 2-10, indicating excellent reversibility. Good reversibility of the conversion reaction is only observed among the ultra-fine SnO_2 materials. More coarse scale SnO_2 does not reverse fully at normal charging rates. The redox peak pair at 0.2V (lithiation) and 0.6V (delithiation) are caused by the reversible alloying process leading to a terminal intermetallic $Li_{22}Sn_5$ phase: $Sn + 4.4Li^+ + 4.4e^- \leftrightarrow Li_{22}Sn_5$. In the first discharging branch of the CV, an exaggerated broad peak at 0-1 V can be observed. This is due to the formation of the solid electrolyte interface (SEI) layer. Figure S3 shows the electrochemical performance of the beseline SnO_2 *vs*. Li, with S3A being the CVs and S3B being the galvanostatic profiles. Two key differences are observed with this coarser structure. First there is substantially more capacity fade during cycling. Second, the conversion peaks are much less pronounced, supporting previous findings regarding the kinetic difficulty of the reaction for larger crystallite sizes.[52]

Figure 2B shows the galvanostatic discharge/charge profiles at $0.5Ag^{-1}$ for cycles 1 – 400. Figure S4 shows the derivative curves (dQ/dV *vs*. V) of those results. The intensity of the anodic 0.6 V peak decreased slightly during the initial 50 cycles and remains constant thereafter, supporting the high reversibility of alloy/dealloy reaction upon extended cycling. According to Figure 2B, a reversible capacity of 1023 $mAhg^{-1}$ is obtained in the second cycle. The galvanostatic data for the identically synthesized pure hydrothermal carbon, tested against Li and against Na, is presented in Figure S5,

6. At 0.5 A/g the capacity of the carbon is ~ 450 $mAhg^{-1}$. Thus a reversible capacity of 1023 $mAhg^{-1}$ is close (95%) to the expected value by rule of mixtures of the two Li active materials (1494 $mAhg^{-1}$ × 0.6 + 450 $mAhg^{-1}$ × 0.4). This ratio proves the full utilization of SnO_2 for both the reversible alloying and conversion reactions.[51]

Beyond cycle 90 the capacity progressively increases, hitting 1367 $mAhg^{-1}$ at cycle 400. A likely explanation for the extra capacity is the formation of a reversible polymer gel on the nanostructured conversion electrode's surface during lithiation, with its consequent dissolution upon delithiation to potentials roughly above 1.5 V. Such a faradic process has been compared to the redox reactions in polymer-based electrochemical capacitors, being highly reversible and imparting a negligible coulombic efficiency penalty.[84,85,86] Similar high CE cycling-induced capacity gains have been reported for a range of conversion oxide electrodes when tested against Li, including SnO_2[51,91] MnO[87] and MoO_2[88]. Since our electrochemical instrument will measure CE with ≥ 1% accuracy, we will refer to computer generated CE values of 100% as being >99%. From cycle 8 onward the CE of C-SnO_2 is > 99%.

Figure 2C shows the cycling results of C-SnO_2 electrodes, with SnO_2 being presented as a baseline. For C-SnO_2 a reversible capacity of 1367 $mAhg^{-1}$ was obtained after 400 cycles at current density of $0.5Ag^{-1}$. At first cycle the coulombic efficiency is 65%, agreeing with previously reported values for SnO_2 tested against Li[52,73]. By the second cycle CE is over 95%, and stabilizes to > 99% from the 8th cycle

onward. Conversely the baseline SnO_2 electrode exhibits only 29% capacity retention after 400 cycles, with CE being never going above 99% through cycling.

The rate performance of C-SnO_2 and SnO_2 is shown in Figure 2D. At current densities of 1.28, 2.56, 5.12, 10.24, 20.48 Ag^{-1}, the C-SnO_2 electrode maintained a capacity of 663, 608, 527, 422 and 255 $mAhg^{-1}$, respectively. Figure 2E shows a rate capability comparison of C-SnO_2 with state-of-the-art previously published electrodes based on both SnO_2(◧) and on Sn (◑). Overall our system is quite promising, being on par with some of the best architectures that have been created. Specifically C-SnO_2 is competitive with potentially more expensive systems based on graphene oxide[89,90], N-doped graphene[51] supports. C-SnO_2 also shows favorable performance in comparison with amorphous carbon - Sn(SnO_2) composites.[31,59,91,92] It is important to point out that for this broad comparison we plotted literature results obtained from a comparable 0.01 V to 3V testing range. We did not include any results for a lower terminal anodic voltage (such as 1.5V) where less reversible capacity is expected.

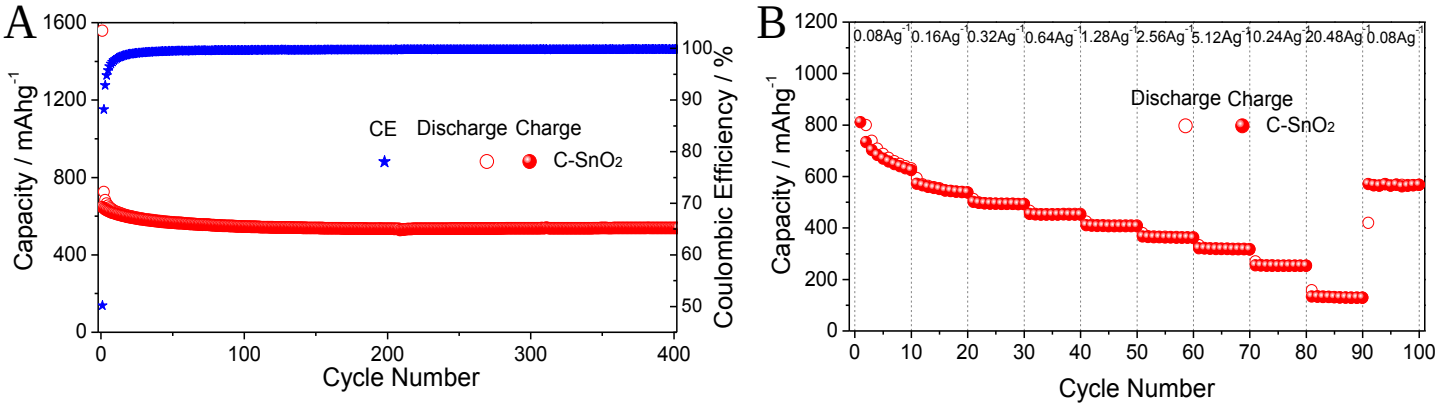

Figure 3: Electrochemical performance of C-SnO_2 versus Li, tested between 0.01 and 1.5 V. (A) Cycling performance of C-SnO_2 (0.5 Ag^{-1}), with corresponding coulombic efficiency (CE) displayed on the right axis. (B) Rate performance of C-SnO_2. The raw galvanostatic discharge/charge profiles are shown in Figures S9A.

We investigated the electrochemical performance of C-SnO_2 against Li at a window of 0.01-1.5V, which may be more (depending on the cathode material) representative of a voltage excursion of an anode in a full battery cell. As will be demonstrated by the XRD and XPS analysis, with a cut-off voltage of 1.5V, Li storage is based on a fully reversible alloying/dealloying reaction and a partially reversible conversion reaction. According to Figure 3A, the initial reversible capacity of the electrode is 633 $mAhg^{-1}$ (at $0.5Ag^{-1}$), retaining 85% of this value after 400 cycles. The 1st cycle coulombic efficiency is 42%, lower than the 65% when charged up to 3V. However, the coulombic efficiency during cycling is good, stabilizing in the > 99% range by cycle 23. At all currents the specific capacity is lower than when the electrodes were charged to 3V, agreeing with findings by ref. [52]. This is due to the incompleteness of the oxide conversion reaction at 1.5V.

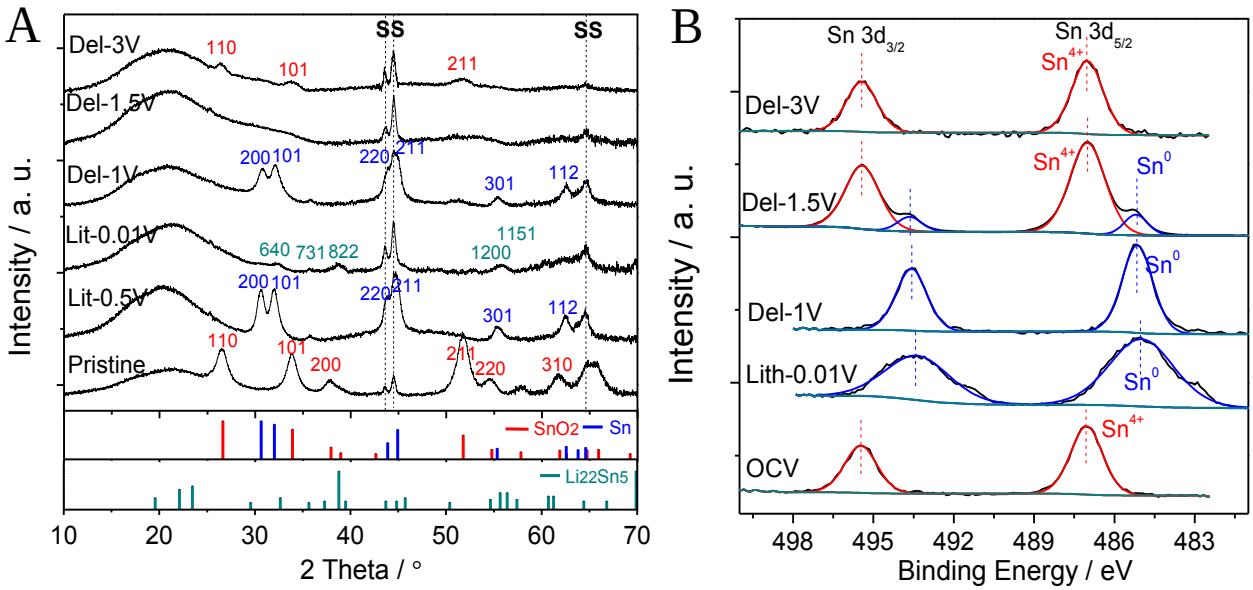

Figure 4: (A) XRD patterns of C-SnO_2 at various cut-off voltages: first lithiation to 0.5V, first lithiation to 0.01 V, first delithiation to 1V, first delithiation to 1.5V, first delithiation to 3V. (B) XPS spectra for Sn 3d levels of C-SnO_2 at open circuit voltage

(prior to testing, used as a baseline), first lithiation to 0.01V, first delithiation to 1V, first delithiation to 1.5V, first delithiation to 3V.

We performed XRD characterization to track the phase transformations in C-SnO_2 *vs.* Li at various cut - off voltages. The electrodes were discharged/charged galvanostatically at ~1/20C (0.05 Ag^{-1}) to the cut-off voltage, and held there until the float current decreased to below 5% of the galvanostatic current. A special sample preparation procedure was employed in order to minimize exposure of the materials to air, oxygen or water vapor. After disassembly in the glove box, the electrodes were firstly washed by DEC to remove remaining salts and EC/DMC, dried in vacuum for 10 minutes and then sealed in plastic tape. Figure S7 shows the XRD pattern for the plastic tape on the stainless steel current collector, without the electrode material, displaying a plastic tape hump at ~22° and the characteristic sharp Bragg peaks for the fcc steel.

The resultant patterns are shown in Figure 4A. When the pristine electrode is first lithiated to 0.5 V Li/Li^+, the reduction reaction of SnO_2 ($SnO_2 + 4Li^+ + 4e^- \rightarrow Sn + Li_2O$) is effectively complete since no SnO_2 signal is detected in the "Lit-0.5V" spectrum. When the electrode is further lithiated down to 0.01 V, Bragg peaks of β-Sn are no longer detectable. Instead, broad peaks ascribed to the $Li_{22}Sn_5$ intermetallic phase are present, with the (640), (731), (822), (12 00) and (11 51) reflections being discernable. The β-Sn peaks re-appear after the electrode is charged back to 1V, indicating full reversibility of the alloying reaction. When charged to 1.5V the β-Sn

peaks disappear, while a weak (110) SnO_2 signal becomes visible, being superimposed on a broad XRD hump associated with the plastic tape. Overall, however, the majority of the material is amorphous at 1.5V. When charged to 3V, the characteristic SnO_2 (110), (101) and (211) peaks are detectable but not well pronounced. This is likely caused by a combination of peak broadening due to the SnO_2 nanocrystalline size and/or a substantial portion of it remaining amorphous.

We performed XPS analysis to track the chemical state of Sn in the C-SnO_2 specimens as a function of voltage. Samples that were lithiated down to 0.01 V were first etched by Ar plasma as to blast off most of the surface SEI which otherwise obscured the analysis. The results for those experiments are presented in Figure 4B, which shows the oxidation state of Sn as a function of voltage. Also shown in the figure are the baseline results for the as-synthesized specimen left at open circuit voltage (OCV). The associated O 1s and C 1s XPS data are shown Figure S8. At 0.01 V, the Sn 3d peaks were present at 493.4 and 485.04 eV, indicating Sn^0 state associated with the $Li_{22}Sn_5$ intermetallic (and/or Li-Sn alloys). Analogously at 1V the Sn 3d peaks also showed primarily the Sn^0 state. After delithiated to 1.5V, the Sn 3d peaks could be deconvoluted into a majority Sn^{4+} and minority Sn^0, indicating that the conversion reaction has proceeded but not entirely to completion. Since no Sn signal with intermediate chemical state was detected, it could be concluded that LiO_2 is reduced directly to SnO_2 and Li. At 3V, the Sn^0 peaks are no longer detectable, indicating full reversibility of the LiO_2 to SnO_2 conversion reaction between 0.01 and

3 V.

Electrochemical Performance and Phase Transformations *vs.* Na

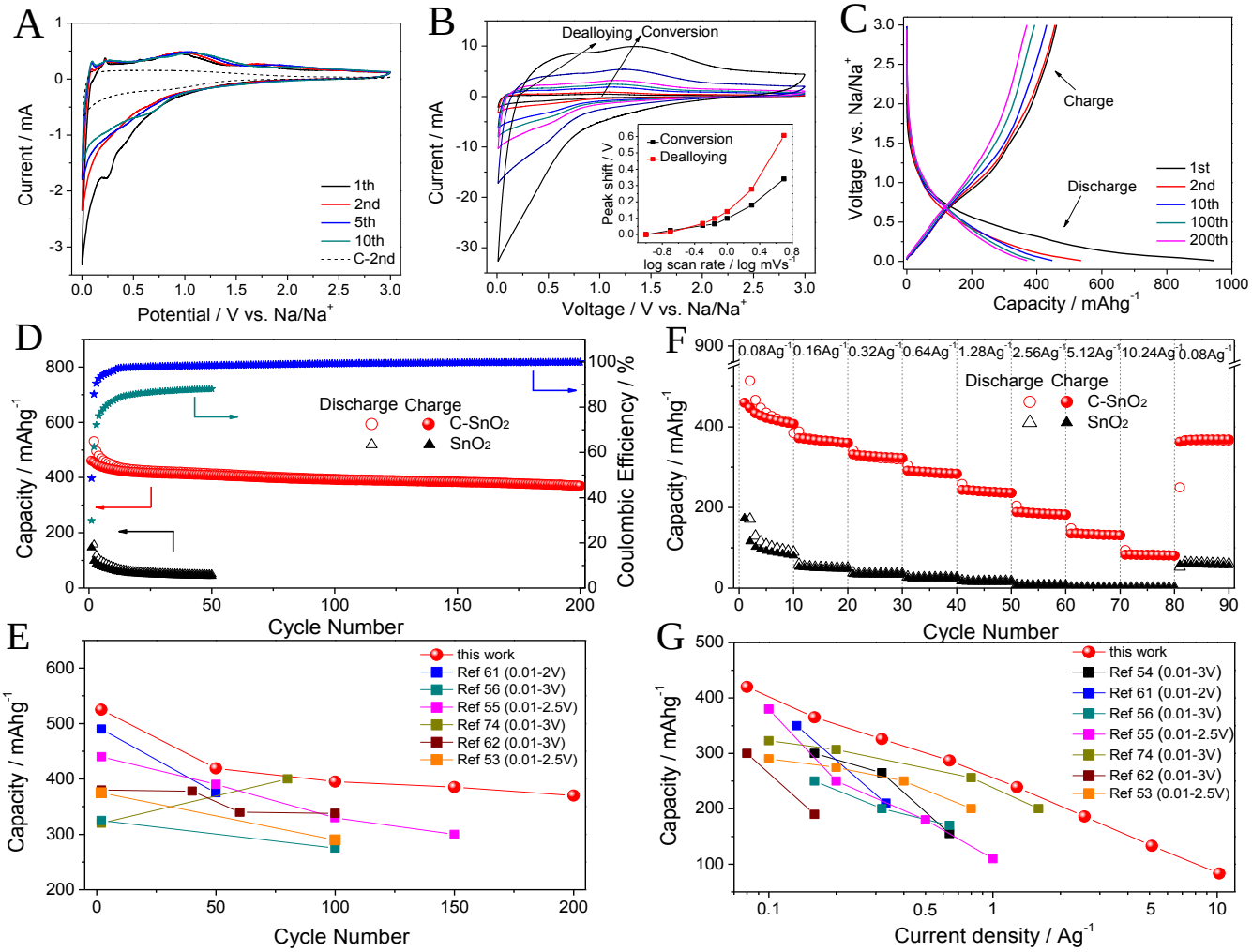

Figure 5: Electrochemical performance of C-SnO_2 and SnO_2 *vs.* Na, tested between 0.01 and 3V. (A) CVs of C-SnO_2 for the cycle 1 - 10, tested at 0.1 mVs^{-1}. (B) CVs of electrode at various scan rates from 0.1 to 5 mVs^{-1}. The shift of the conversion/dealloying peaks as function of scan rate (inset). (C) Galvanostatic discharge/charge profiles of C-SnO_2, tested at 80 mAg^{-1}. (D) Cycling performance of C-SnO_2 and SnO_2 (0.08 Ag^{-1}), with corresponding CE displayed on the right axis. (F) Rate performance of C-SnO_2 and SnO_2 electrodes. (E) and (G) Cycling capacity retention and rate capability comparison of C-SnO_2 with state-of-the-art SnO_2 based NIBs anodes from literature.

Figure 5A shows the CVs of C-SnO_2 during the first 10 cycles, as well as the 2nd

cycle CV of the pure carbon baseline. It may be seen that compared to the CV data for Li, the redox peaks for the Na conversion and alloying reactions are much broader and washed out. The peaks' overall intensity is also lower for Na than for Li, which will be shown to agree well with a substantially lower capacity. In the cathodic portion of the scan, a broad peak initiates near 1.7V *vs*. Na/Na^+, with its intensity increasing all the way down to full discharge. As will be demonstrated through XRD analysis, this peak corresponds primarily to the oxide conversion reaction, with the Sn-Na alloying reaction not running to completion. As may be seen from Figure S5, Na insertion into the carbon phase contributes to the broad "background" of the CV curve, but does not add any sharp redox peaks. In the first cycle, the formation of SEI also contributes to the total CV current, producing the small hump at around 0.4V.[27,55]

In the anodic portion of the CV, the first small peak appears at ~ 0.1 V and is ascribed to the Na extraction from the carbon phase.[16] The small sharp peaks at ~ 0.23 and ~ 0.56 V have been ascribed to the progressive dealloying reactions from $Na_{15}Sn_4$ (crystalline) to Na_9Sn_4 (amorphous) and then to NaSn (amorphous) and to $NaSn_5$ (amorphous).[27,74] Judging from the alloying peaks' small relative intensity, it is unlikely that all of the Sn in the electrode transforms accordingly. XRD analysis will demonstrate that at 0.01V a notable fraction of the material remains as β-Sn, while complementary HRTEM will highlight a co-presence of small and isolated $Na_{15}Sn_4$ intermetallics. In the anodic portion of the CV, the expected position of the final dealloying peak (i.e. formation of β-Sn) overlaps with two other broad anodic peaks.

These will be shown to be associated with the Na_2O to SnO_2 conversion reaction that proceeds through an intermediate SnO phase. The CV curve of the baseline SnO_2 (Figure S10A) shows very poorly defined redox peaks. As the XRD results will demonstrate, in the coarser baseline SnO_2 both conversion and alloying are kinetically difficult. In that system the total current quickly degrades with cycle number.

We further analyzed the sodiation kinetics of C-SnO_2 by performing CV tests at various scan rates, 0.1 – 5 mVs^{-1}. Those results are shown in Figure 5B. It can be observed from the anodic portion of the graph that both the dealloying and the conversion reaction peaks shift to higher voltages with increasing scan rate, but that the alloying peak shows a larger shift than the conversion peak. The magnitude of the shift (*i.e.* the overpotential) for a given reaction is indicative of its kinetic feasibility, and demonstrates that Na-Sn alloying is more difficult than the conversion.

Figure 5C shows the galvanostatic charge/discharge profiles of C-SnO_2 electrode at current density of 0.08 Ahg^{-1}. A capacity of 946 $mAhg^{-1}$ was obtained in the first sodiation. A reversible capacity of 459 $mAhg^{-1}$ is obtained at cycle 1, resulting in a CE of 48.5%. As may be observed from Figure S5, the sodiation capacity of baseline amorphous carbon is lower than for lithiation. For Na at cycle 1 the reversible capacity of the baseline carbon is 195 $mAhg^{-1}$, while at cycle 500 it is 95 $mAhg^{-1}$. Conversely with Li these values are 450 $mAhg^{-1}$ and 250 $mAhg^{-1}$. These results show that the exact same SnO_2 based material and the exact same carbon tested against Na

will display less than half the reversible capacity as when tested against Li.

Figure 5D shows the cycling capacity retention performance of C-SnO_2 and of the baseline SnO_2. The electrodes were tested in the voltage at current density of 0.08 Ag^{-1}. The C-SnO_2 electrode displayed excellent cyclability; a specific capacity of 372 $mAhg^{-1}$ was obtained after 200 full charge/discharge cycles, which is 81% of the initial charge value. By contrast, the reversible capacity of baseline SnO_2 rapidly decays, going from 147 to 49 $mAhg^{-1}$ after 50 cycles. Figure 5D also shows the cycling CE for both materials. In C-SnO_2 the CE grows to over 90% by the 3rd cycle, and stabilized to 98% to >99% from cycle 20 onward. The cycling CE of SnO_2 is much lower, never going above 90%.

Figure 5E shows a comparison of the cycling performance of C-SnO_2 to the state-of-the-art nanomaterials based on SnO_2.[53,54,55,56,61,62,74] In the figure, the data legend lists the exact testing voltage window along with the associated citation. The anodic upper limit varied from study to study, being in the 2 – 3 V range. Examining previously published results one concludes that there does not appear to be a correlation in the capacity versus cycle number values with the upper anodic limit, as long as it is at or above 2V. Rather, performance seems to be dictated by the microstructure of the electrode. We did not include any metallic Sn results from literature, as this would not be an appropriate comparison. Since sodiation/lithiation of metallic Sn does not involve conversion reactions (apart from the native surface

oxide), one would be essentially comparing "apples to oranges" in terms of both phase transformations and the performance measures.

As may be observed, C-SnO_2 is among the most favorable both in terms of the total reversible capacity and the cycling capacity retention. It is important to note that the cyclability performance in this work was achieved using normal PVDF binder and practical organic electrolyte (*i.e.* 1 mol $NaClO_4$ in EC/DEC mixture). We did not employ any SEI stabilizing additive (*e.g.* fluoroethylene carbonate, FEC), which would be expected to further boost the cycling performance.[32,55,93,94]

A straightforward explanation for the superior cycling performance of C-SnO_2 lies in its monocoque microstructure that is distinct from the usual nanocomposites consisting of particulate assemblies. During cycling the carbon frame carries the sodiation/lithiation stresses while preventing cycling-induced agglomeration of the individual crystals. Figure S11 show (A-C) TEM micrographs of C-SnO_2 showing the microstructure at open circuit potential (prior to cycling), sodiated once to 0.01V and desodiated once to 3V. The figure also shows corresponding histograms for the size of the active SnO_2 nanocrystal assemblies (not individual crystallites) at each condition. The histograms were obtained using Gwddion software from ~80 assemblies on 5 separate micrographs. According the measured size distribution the initial SnO_2 crystallite assembly mean diameter is 29 nm. The cluster diameter is 32 nm at full sodiation, and is the same after full desodiation. This demonstrates that while the

expansion of the active SnO_2 phases is upwards of several hundred percent (exact value will depend on the degree of completion of the alloying and conversion reactions), the surrounding carbon matrix acts as a buffer to minimize the macroscopic strain on the electrode and prevents its decrepitation. As may be seen from the HRTEM image in Figure 1E the carbon engulfs the individual SnO_2 nanocrystallites, which is expected to minimize their agglomeration during cycling.

Figure 5F shows the capacity of C-SnO_2 and of SnO_2 at various current densities. Overall the C-SnO_2 electrode exhibits outstanding rate performance, far superior to SnO_2 that has effectively negligible capacity at higher rates. The C-SnO_2 possesses the dual advantage of the carbon frame and the sub 5 nm - scale of the individual SnO_2 crystallites. The Na active carbon frame imparts excellent electrical conductivity to the electrode and allows for rapid diffusion of Na and Li ions. The fine scale of the crystallites shortens the diffusion distance, reducing the time needed for both the alloying and the conversion reactions. Since the diffusion time is proportional to the diffusion length squared, the sub 5 nm crystallites in C-SnO_2 will have a tremendous kinetic advantage over the 50 nm crystallites in baseline SnO_2. For C-SnO_2, capacities of 187, 136 and 80 $mAhg^{-1}$ are obtained at current densities of 2.56, 5.12 and 10.28 Ag^{-1}. A comparison of our materials rate capability with the best SnO_2 materials from literature is shown in Figure 5G. In the range of 2 – 3 V, there does not appear to be a correlation in the capacity versus current density values with the upper anodic limit. Previously published architectures include SnO_2@graphene nanocomposites,[54,55]

SnO_2 anchored CNT,[61] octahedral SnO_2 nanocrystals.[62] It may be observed that overall the C-SnO_2 electrode looks quite favorable.

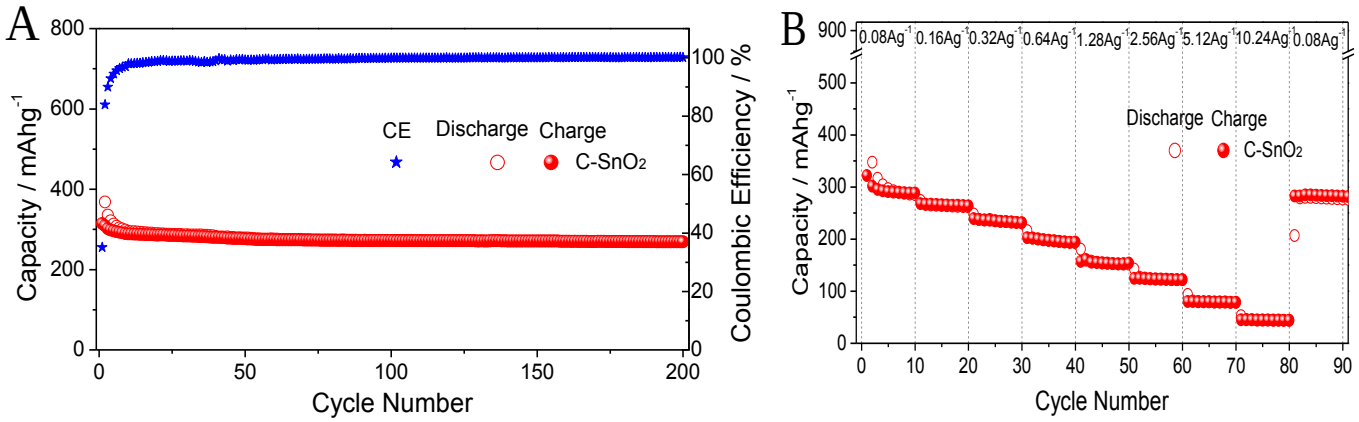

Figure 6: Electrochemical performance of C-SnO_2 versus Na, tested between 0.01 and 1.5 V. (A) Cycling performance (0.08 Ag^{-1}), with corresponding CE displayed on the right axis. (B) Rate performance. The raw galvanostatic data are shown in Figures S9B.

Figure 6 shows the cycling and the rate performance of C-SnO_2 electrodes against Na, tested between 0.01-1.5V. As shown in Figure 6A, although C-SnO_2 exhibits a lower total reversible capacity than when it is charged to 3V, the cyclability is actually improved. At cycle 1 the reversible capacity is 314 mAh/g, while at cycle 200 it is 270 mAh/g, i.e. only a 86 % degradation. We attribute enhanced cycling to a greater structural stability of the SEI with the lower voltage window. This explanation makes the most sense if the SEI is considered to be a dynamically evolving product, which partially dissolves and/or changes in composition/structure during anodic polarization. The superior cycling up to 1.5V also gives great hope for the performance of a full sodium ion battery cell, where the anodic swing on the negative electrode will be closer to that range. The coulombic efficiency of the electrode increased to 90% by the 3rd cycle, to over 98% by the 12th cycle, and > 99 % from the

21th cycle onwards. As shown in Figure 6B, capacities of 150, 125 and 80 $mAhg^{-1}$ were obtained at current densities of 1.2, 2.5 and 5 Ag^{-1}.

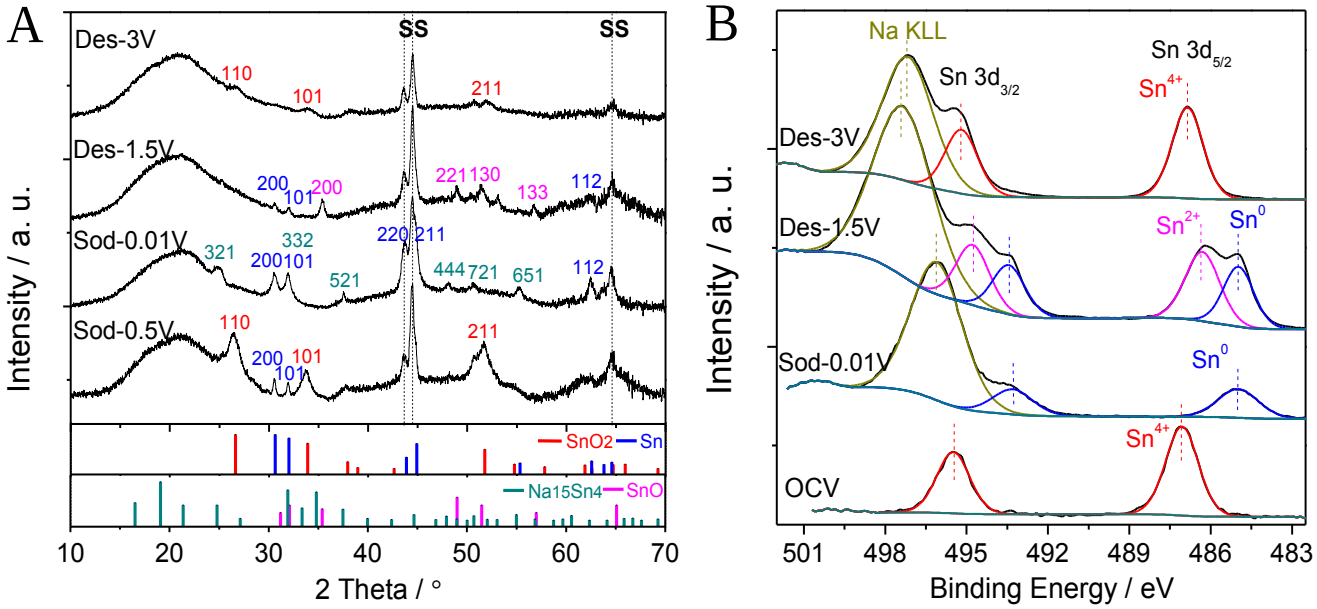

Figure 7: (A) XRD patterns of C-SnO_2 at various cut-off voltages: first sodiation to 0.5V, first sodiation to 0.01 V, first desodiation to 1.5V, first desodiation to 3V. (B) XPS spectra for Sn 3d levels of C-SnO_2 at open circuit voltage, first sodiation to 0.01 V, first desodiation to 1.5V, first desodiation to 3V.

We performed XRD characterization to track the phase transformations in C-SnO_2 *vs.* Na at various cut - off voltages, with the resultant patterns being shown in Figure 7A. Upon first sodiation to 0.5 V new peaks ascribed to β-Sn appeared besides the original SnO_2 peaks. This change indicates the occurrence of conversion reaction $SnO_2 + 4Na^+ + 4e^- \rightarrow Sn + Na_2O$. The Na_2O phase had been reported to be amorphous, which explains the lack of associated Bragg peaks. As the electrode was further discharged down to 0.01 V the SnO_2 phase completely disappeared, while peaks associated with the $Na_{15}Sn_4$ intermetallic arose. However at 0.01 V the crystalline Sn peaks remained intense, indicating that the alloying reaction $Sn + 3.75\ Na^+ + 3.75\ e^- \rightarrow Na_{15}Sn_4$ is not fully completed. The fact that crystalline Sn is present

means that some portion of the material has not even sodiated to one of the intermediate amorphous Na-Sn compositions[60,75].

We attribute the unreacted Sn to be the root cause of the much lower capacity of C-SnO_2 with Na than with Li: A substantial portion of the initial SnO_2 phase that is reduced to metallic Sn by the Na does not further participate in the sodiation reaction. This is most likely due to the lower diffusivity of Na in Sn, as well as perhaps due to sluggish interfacial reaction kinetics. Another contributing factor to the incomplete reaction may include poor diffusion of Na through the Na_2O shell that surrounds the metallic Sn after the conversion reaction, as compared to diffusion of Li through the Li_2O shell. A thicker and structurally different SEI will also block or reduce the rates of sodiation *versus* lithiation in the same material. It is important to point out that we did not employ the most stable electrolyte available (one containing FEC). Thus the contribution of the SEI layer on both the C-SnO_2 electrode and on the Na counter electrode may be significant enough to overshadow the intrinsic diffusivity differences.

The same XRD characterization was performed on baseline SnO_2 electrodes. The resultant patterns are shown in Figure S12. The β-Sn peaks with high intensity in Sod-0.01V spectrum indicate the large amount of unalloyed Sn phase after the first sodiation process. When the electrode was desodiated to 1.5 V the $Na_{15}Sn_4$ peaks disappeared, to be replaced by an intermediate orthorhombic SnO phase. This is a

distinct difference from the case for C-SnO_2 with Li, where the conversion reaction proceeds from LiO_2 to SnO_2 with no intermediates. Relatively weak crystalline β-Sn peaks were also present at 1.5 V. When desodiated to 3 V the β-Sn peaks completely disappeared, indicating that the material is back to being oxidized. At 3 V there is some evidence of rutile SnO_2, although just like the case for SnO_2 with Li, much of the reformed oxide is nanocrystalline and/or amorphous.

XPS tests were performed to track the chemical state of Sn in C-SnO_2 electrode during sodiation/desodiation. The results for those experiments are presented in Figure 7B and in Figure S13 for O 1s and C 1s. After discharging to 0.01V from OCV, the Sn 3d peaks shifted to 485 and 493.2 eV, indicating the complete reduction of Sn^{4+} to Sn^0 in the first sodiation process. At 1.5V the Sn 3d peaks are deconvoluted into two components. According to the binding energies, there are both Sn^0 and Sn^{2+} states detected at this voltage, agreeing with the XRD results. After further desodiation to 3V, the Sn 3d peaks shifted to the Sn^{4+} position, characterizing the reformation of SnO_2.

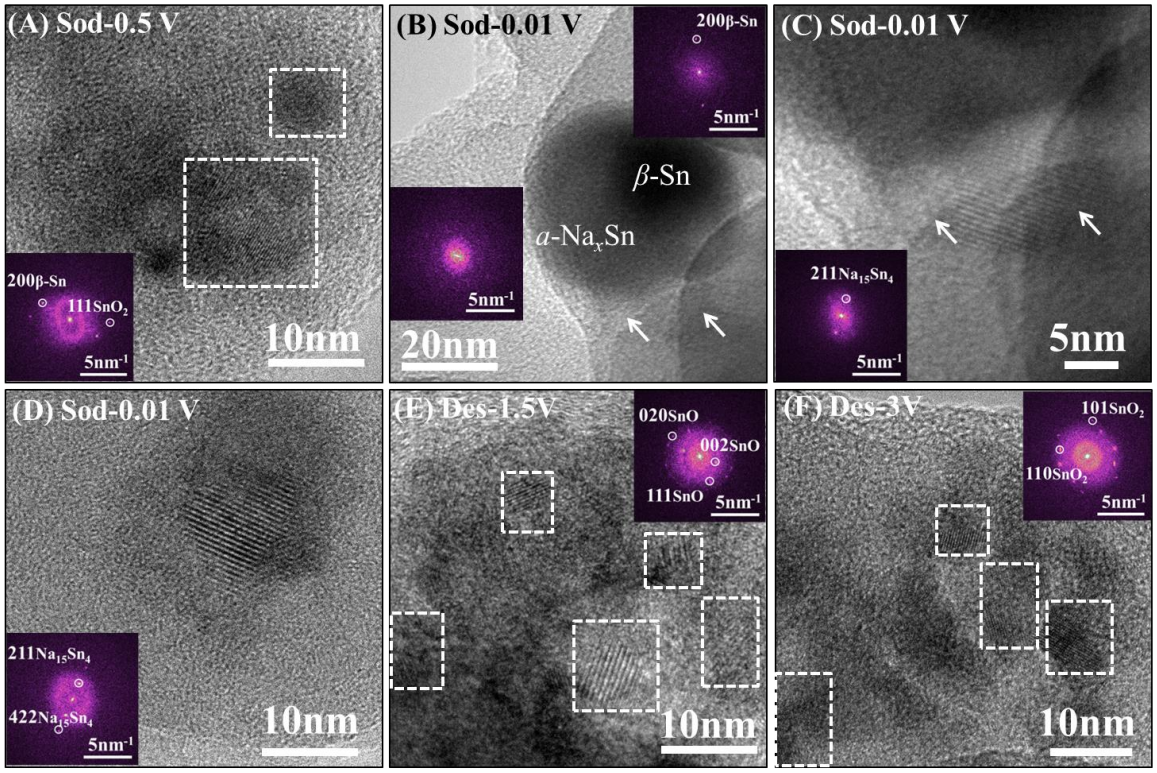

Figure 8: HRTEM micrographs of C-SnO_2 electrodes with corresponding indexed FFT patterns corresponding to regions in white squares. (A) first sodiation to 0.5 V. (B,C,D) first sodiation to 0.01 V. The regions indicated by double arrows in (B) (C) are the same region with different magnification. (E) first desodiation to 1.5V, (F) first desodiation to 3V.

Figure 8 shows HRTEM micrographs of C-SnO_2 electrodes with corresponding indexed FFT patterns. For these specimens the electrodes were discharged/charged galvanostatically (0.025 Ag^{-1}) to the cut-off voltages, and held there until the float current decreased to below 5% of the galvanostatic current. Results are shown after the first sodiation to 0.5 V, after the first sodiation to 0.01 V, after the first desodiation to 1.5V and after the first desodiation to 3V. When sodiated to 0.5 V we observe both crystalline β-Sn and SnO_2 interspersed in an amorphous matrix. At 0.01 V, unreacted β-Sn is still present. Here it is surrounded by a shell of amorphous high atomic mass material (distinct from amorphous carbon) that is likely some intermediate Na_xSn alloy. Small and isolated $Na_{15}Sn_4$ crystallites are observed, although they by no means

constitute the majority of the Sn in the material. For instance, one such intermetallic is marked in Figure 8B (indicated by double arrows), with a higher magnification image of the marked area being shown in Figure 8C. The lattice fringes of this crystallite correspond to (211) $Na_{15}Sn_4$. Another isolated $Na_{15}Sn_4$ crystallite is shown in Figure 8D. The electrode desodiated to 1.5 V shows a distribution sub-10 nm SnO crystallites as well as an amorphous matrix. When desodiated to 3 V the crystalline phase returns to SnO_2.

Conclusions

To summarize, we used a hydrothermal self-assembly method to create a nanocomposite based on sub- 5nm SnO_2 nanocrystallites in carbon that had excellent bifunctionality as a lithium and a sodium ion battery anode. Especially when tested against Na, the material displayed capacity, cyclability and high-rate capability that are promising relative to published results. Additionally we provide a systematic comparison examination of the sodiation *versus* the lithiation related phase transformations in nanostructured SnO_2, and establish the fundamental microstructural causes for the much lower capacity observed with Na as compared to Li.

References

1 M. Armand, J. M. Tarascon, *Nature*, 2008, **451**, 652-657.

2 J. H. Pikul, H. G. Zhang, J. Cho, P. V. Braun, W. P. King, *Nat. Commun.*, 2013, **4**.

3 M. S. Whittingham, *Chem. Rev.* 2014, **114**, 11414-11443.

4 N. Yabuuchi, K. Kubota, M. Dahbi, S. Komaba, *Chem. Rev.*, 2014, **114**, 11636-11682.

5 V. Palomares, P. Serras, I. Villaluenga, K. B. Hueso, J. Carretero-Gonzalez, T. Rojo, *Energy Environ. Sci.*, 2012, **5**, 5884-5901.

6 V. Palomares, M. Casas-Cabanas, E. Castillo-Martinez, M. H. Han, T. Rojo, *Energy Environ. Sci.*, 2013, **6**, 2312-2337.

7 S. W. Kim, D. H. Seo, X. H. Ma, G. Ceder, K. Kang, *Adv. Energy Mater.*, 2012, **2**, 710-721.

8 M. D. Slater, D. Kim, E. Lee, C. S. Johnson, *Adv. Funct. Mater.*, 2013, **23**, 947-958.

9 L. Wang, Y. H. Lu, J. Liu, M. W. Xu, J. G. Cheng, D. W. Zhang, J. B. Goodenough, *Angew. Chem. Int. Edit.*, 2013, **52**, 1964-1967.

10 B. Koo, S. Chattopadhyay, T. Shibata, V. B. Prakapenka, C. S. Johnson, T. Rajh, E. V. Shevchenko, *Chem. Mater.*, 2013, **25**, 245-252.

11 M. Han, E. Gonzalo, G. Singh, T. Rojo, *Energy Environ. Sci.*,2015, **8**, 81-102.

12 N. Yabuuchi, M. Kajiyama, J. Iwatate, H. Nishikawa, S. Hitomi, R. Okuyama, R. Usui, Y. Yamada, S. Komaba, *Nat. Mater.*, 2012, **11**, 512-517.

13 Y. Jung, C. Lim, D. Kim, *J. Mater. Chem. A*, 2013, **1**, 11350-11354.

14 S. Li, Y. Dong, L. Xu, X. Xu, L. He, L. Mai, *Adv. Mater.*, 2014, **26**, 3545-53.

15 W. Song, X. Cao, Z. Wu, J. Chen, K. Huangfu, X. Wang, Y. Huang, X. Ji, *Phys. Chem. Chem. Phys.*, 2014,**16**, 17681-17687.

16 J. Ding, H. L. Wang, Z. Li, A. Kohandehghan, K. Cui, Z. W. Xu, B. Zahiri, X. H. Tan; E. M. Lotfabad, B. C. Olsen, D. Mitlin, ACS *Nano*, 2013, **7**, 11004-11015.

17 W. Luo, J. Schardt, C. Bommier, B. Wang, J. Razink, J. Simonsen, X. Ji, *J. Mater. Chem. A*,2013, **1**, 10662.

18 J. Ding, H. Wang, Z. Li, K. Cui, D. Karpuzov, X. Tan, A. Kohandehghan, D. Mitlin, *Energy Environ. Sci.*, 2015, DOI: 10.1039/c4ee02986k.

19 K. Tang, L. J. Fu, R. J. White, L. H. Yu, M. M. Titirici, M. Antonietti, J. Maier, *Adv. Energy Mater.*, 2012, **2**, 873-877.

20 H. Cha, H. Jeong, J. Kang, *J. Mater. Chem. A*, 2014, **2**, 5182-5186.

21 Y. Xu, E. M. Lotfabad, H. L. Wang,; B. Farbod, Z. W. Xu,; A. Kohandehghan, D. Mitlin, *Chem. Commun.*, 2013, **49**, 8973-8975.

22 P. Senguttuvan, G. Rousse, V. Seznec, J. M. Tarascon, M. R. Palacin, *Chem.*

Mater., 2011, **23**, 4109-4111.

23 H. L. Pan, X. Lu, X. Q. Yu, Y. S.Hu, H. Li, X. Q. Yang, L. Q. Chen, *Adv. Energy Mater.*, 2013, **3**, 1186-1194.

24 Y. Zhu, P. Nie, L. Shen, S. Dong, Q. Sheng, H. Li, H. Luo, X. Zhang, *Nanoscale*, 2014, DOI:10.1039/C4NR05242K.

25 L. Baggetto, H. Y. Hah, J. C. Jumas, C. E. Johnson, J. A. Johnson, J. K. Keum, C. A. Bridges, G. M. Veith, *J. Power Sources*, 2014, **267**, 329-336.

26 L. F. Xiao, Y. L. Cao, J. Xiao, W. Wang, L. Kovarik, Z. M. Nie, J. Liu, *Chem. Commun.*, 2012, **48**, 3321-3323.

27 Y. H. Xu, Y. J. Zhu, Y. H. Liu, C. S. Wang, *Adv. Energy Mater.* 2013, **3**, 128-133.

28 B. Farbod, K. Cui, W. P. Kalisvaart, M. Kupsta, B. Zahiri, A. Kohandehghan, E. M. Lotfabad, Z. Li, E. J. Luber, D. Mitlin, ACS *Nano*, 2014, **8**, 4415-4429.

29 L. Baggetto, K. J. Carroll, H. Y. Hah, C. E. Johnson, D. R. Mullins, R. R. Unocic, J. A. Johnson, Y. S. Meng, G. M. Veith, *J. Phys. Chem. C.*, 2014, **118**, 7856-7864.

30 V. Kulish, O. Malyi, M. Ng, Z. Chen, S. Manzhos, P. Wu, *Phys. Chem. Chem. Phys.*, 2014, **16**, 4260-4267.

31 Y. H. Xu, Q. Liu, Y. J. Zhu, Y. H. Liu, A. Langrock, M. R. Zachariah, C. S. Wang, *Nano Lett.*, 2013, **13**, 470-474.

32 D. Bresser, F. Mueller, D. Buchholz, E. Paillard, S. Passerini, *Electrochim. Acta*, 2014, **128**, 163-171.

33 C. K. Chan, H. L. Peng, G. Liu, K. McIlwrath, X. F. Zhang, R. A. Huggins, Y. Cui, *Nat. Nanotechnol.*, 2008, **3**, 31-35.

34 X. Zhu, H. Chen, Y. Wang, L. Xia, Q. Tan, H. Li, Z. Zhong, F. Su, XS. Zhao, *J. Mater. Chem. A*, 2013, **14**, 4483-4489.

35 Y. Yao, N. Liu, M. T. McDowell, M. Pasta, Y. Cui, *Energy Environ. Sci.*, 2012, **5**, 7927-7930.

36 M. H. Seo, M. Park, K. T. Lee, K. Kim, J. Kim, J. Cho, *Energy Environ. Sci.*, 2011, **4**, 425-428.

37 T. Ramireddy, M. Rahman, T. Xing, Y. Chen, A. M. Glushenkov, *J. Mater. Chem. A*, 2014, **2**, 4282-4291.

38 A. Darwiche, C. Marino, M. T. Sougrati, B. Fraisse, L. Stievano, L. Monconduit, *J. Am. Chem. Soc.*, 2012, **134**, 20805-20811.

39 Y. Wang, F. Su, JY. Lee, XS. Zhao, *Chem. Mater.*, 2006, **18**, 1347-1353.

40 X. Wang, X. Q. Cao, L. Bourgeois, H. Guan, S. M. Chen, Y. T. Zhong, D. M. Tang, H. Q. Li, T. Y. Zhai, L. Li, Y. Bando, D. Golberg, *Adv. Funct. Mater.*, 2012, **22,** 2682-2690.

41 H. W. Song, N. Li, H. Cui, C. X. Wang, *J. Mater. Chem. A*, 2013, **1**, 7558-7562.

42 J. Liu, H. G. Zhang, J. Wang, J. Cho, J. H. Pikul, E. S. Epstein, X. Huang, J. Liu, W. P. King, P. V. Braun, *Adv. Mater.*, 2014, **26**, 7096-101.

43 N. Yesibolati, M. Shahid, W. Chen, M. N. Hedhili; M. C. Reuter, F. M. Ross, H. N. Alshareef, *Small*, 2014, **10**, 2849-2858.

44 D. W. Su, X. Q. Xie, G. X. Wang, *Chem-Eur. J.*, 2014, **20**, 3192-3197.

45 M. Shimizu, H. Usui, H. Sakaguchi, *J. Power Sources*, 2014, **248**, 378-382.

46 M. Shahid, N. Yesibolati, M. C. Reuter, F. M. Ross, Whittingham, *J. Power Sources*, 2014, **263**, 239-245.

47 H. Bryngelsson, J. Eskhult, L. Nyholm, M. Herranen, O. Alm, K. Edstrom, *Chem. Mater.*, 2007, **19**, 1170-1180.

48 V. Aravindan, P. Vickraman, *Solid State Sci.*, 2007, **9**, 1069-1073.

49 X. Fan, J. Shao, X. Xiao, X. Wang, S. Li, H. Ge, L. Chen, C. S. Wang, *J. Mater. Chem. A*, 2014, **2**, 18367-18374.

50 L. Zhang, H. Wu, B. Liu, X. Lou, *Energy Environ. Sci.*, 2014, **7**, 1013-1017.

51 X. S. Zhou, L. J. Wan, Y. G. Guo, *Adv. Mater.*, 2013, **25**, 2152-2157.

52 Z. X. Chen, M. Zhou, Y. L. Cao, X. P. Ai, H. X. Yang, J. Liu, *Adv. Energy Mater.*, 2012, **2**, 95-102.

53 S. Li, Y. Wang, J. Qiu, M. Ling, H. Wang, W. Martens, S. Zhang, *RSC Adv.*, 2014, **4**, 50148-50152.

54 D. W. Su, H. J. Ahn, G. X. Wang, *Chem. Commun.*, 2013, **49**, 3131-3133.

55 Y. X. Wang, Y. G. Lim, M. S. Park, S. L. Chou, J. H. Kim, H. K. Liu, S. X. Dou, Y. J. Kim, *J. Mater. Chem. A*, 2014, **2**, 529-534.

56 X. Xie, D. Su, J. Zhang, S. Chen, A. Mondal, G. Wang, *Nanoscale*, 2015, DOI: 10.1039/C4NR0754B.

57 J. Y. Huang,; L. Zhong,; C. M. Wang,; J. P. Sullivan,; W. Xu,; L. Q. Zhang,; S. Mao, X.; N. S. Hudak,; X. H. Liu,; A. Subramanian,; H. Y. Fan,; L. A. Qi,; A. Kushima,; J. Li, *Science*, 2010, **330**, 1515-1520.

58 A. M. Nie, L. Y. Gan, Y. C. Chong, H. Asayesh-Ardakani, Q. Q. Li, C. Z. Dong, R. Z. Tao, F. Mashayek, H. T. Wang, U. Schwingenschlogl, R. F. Klie, R. S. Yassar, ACS *Nano*, 2013, **7**, 6203-6211.

59 G. M. Zhou, D. W. Wang, L. Li, N. Li, F. Li, H. M. Cheng, *Nanoscale*, 2013, **5**, 1576-1582.

60 L. D. Ellis, T. D. Hatchard, M. N. Obrovac, *J. Electrochem. Soc.*, 2012, **159**, A1801-A1805.

61 Y. Wang, D. W. Su, C. Y. Wang, G. X. Wang, *Electrochem. Commun.*, 2013, **29**, 8-11.

62 D. W. Su, C. Y. Wang, H. Ahn, G. X. Wang, *Phys. Chem. Chem. Phys.*, 2013, **15**, 12543-12550.

63 J. Park, J. W. Park, J. H. Han, S. W. Lee, K. Y. Lee, H. S. Ryu, K. W. Kim, G. X. Wang, J. H. Ahn, H. J. Ahn, *Mater. Res. Bull.*, 2014, **58**, 186-189.

64 M. Shahid, N. Yesibolati, M. C. Reuter, F. M. Ross, H. N. Alshareef, *J. Power Sources*, 2014, **263**, 239-245.

65 W. J. Zhang, *J. Power Sources*, 2011, **196**, 13-24.

66 H. X. Zhang, C. Feng, Y. C. Zhai, K. L. Jiang, Q. Q. Li, S. S. Fan, *Adv. Mater.*, 2009, **21**, 2299-2304.

67 Y. Wang, H. C. Zeng, J. Y. Lee, *Adv. Mater.*, 2006, **18**, 645-649.

68 S. M. Paek, E. Yoo, I. Honma, *Nano Lett.*, 2009, **9**, 72-75.

69 X. D. Huang, X. F. Zhou, L. Zhou, K. Qian, Y. H. Wang, Z. P. Liu, C. Z. Yu, *ChemphysChem*, 2011, **12**, 278-281.

70 C. A. Bonino, L. W. Ji, Z. Lin, O. Toprakci, X. W. Zhang, S. A. Khan, *ACS Appl. Mater. Inter.*, 2011, **3**, 2534-2542.

71 X. Zhang, J. Liang, G. X. Gao, S. J. Ding, Z. L. Yang, W. Yu, B. Q. Li, *Electrochim. Acta*, 2013, **98**, 263-267.

72 L. Zhang, G. Q. Zhang, H. B. Wu, L. Yu, X. W. Lou, *Adv. Mater.*, 2013, **25**, 2589-2593.

73 M. He, L. X. Yuan, X. L. Hu, W. X. Zhang, J. Shu, Y. H. Huang, *Nanoscale*, 2013, **5**, 3298-3305.

74 Y. Zhang, J. Xie, S. Zhang, P. Zhu, G. Cao, X. Zhao, *Electrochim. Acta*, 2015, **151**, 8-15.

75 J. W. Wang, X. H. Liu, S. X. Mao, J. Y. Huang, *Nano Lett.*, 2012, **12**, 5897-5902.

76 X. W. Lou, C. Yuan, L. A. Archer, *Small*, 2007, **3**, 262-265.

77 W. S. Kim, Y. Hwa, H. C. Kim, J. H. Choi, H. J. Sohn, S. H. Hong, *Nano Res.*, 2014, **7**, 1128-1136.

78 A. Z. Adamyan, Z. N. Adamian, V. M. Aroutiounian, *Sensors*, 2003, **3**, 438-442.

79 X. W. Lou, Y. Wang, C. Yuan, J. Lee, L. A. Archer, *Adv. Mater.*, 2006, **18**, 2325-2329.

80 S. Ikeda, K. Tachi, Y. H. Ng, Y. Ikoma, T. Sakata, H. Mori, T. Harada, M. Matsumura, *Chem. Mater.*, 2007, **19**, 4335-4340.

81 X. W. Lou, J. S. Chen, P. Chen, L. A. Archer, *Chem. Mater.* 2009, **21**, 2868-2874.

82 C. Wang, Y. Zhou, M. Y. Ge, X. B. Xu, Z. L. Zhang, J. Z. Jiang, *J. Am. Chem. Soc.*, 2010, **132**, 46-47.

83 T. Egami, S. J. L. Billinge, Underneath the Bragg Peaks: Structural analysis of Complex Materials, Elsevier Ltd., 2003.

84 A. Ponrouch, P. L. Taberna, P. Simon, M. R. Palacin, *Electrochim. Acta*, 2012, **61**, 13-18.

85 S. Grugeon, S. Laruelle, L. Dupont, J.-M. Tarascon, *Solid State Sciences*, 2003, **5**, 895-940.

86 S. Laruelle, S. Grugeon, P. Poizot, M. Dolle, L. Dupont, J.-M. Tarascon, *J. Electrochem. Soc.*, 2002, **149**, 627-634.

87 H. L. Wang, Z. W. Xu, Z. Li, K. Cui, J. Ding, A. Kohandehghan, X. H. Tan, B. Zahiri, B. C. Olsen, C. M. B. Holt, D. Mitlin, *Nano Lett.*, 2014, **14**, 1987-1994.

88 Z. W. Xu, H. L. Wang, Z. Li, A. Kohandehghan, J. Ding, J. Chen, K. Cui, D. Mitlin, *J. Phys. Chem. C*, 2014, **118**, 18387-18396.

89 Y. Chen, B. Song, R. Chen, L. Lu, J. Xue, *J. Mater. Chem. A*, 2014, **2**, 5688-5695.

90 F. Han, W. Li, M. Li, A. Lu, *J. Mater. Chem*, 2012, **22**, 9645-9651.

91 Y. H. Xu, J. C. Guo, C. S. Wang, *J. Mater. Chem.*, 2012, **22**, 9562-9567.

92 X. W. Lou, C. M. Li, L. A. Archer, *Adv. Mater.*, 2009, **21**, 2536-2539.

93 K. Dai, H. Zhao, Z. Wang, X. Song, V. Battaglia, G. Liu, *J. Power Sources*, 2014, **263**, 276-279.

94 S. A. Webb, L. Baggetto, C. A. Bridges, G. M. Veith, *J. Power Sources*, 2014, **248**, 1105-1117.